1 **The mechanics of shallow magma reservoir outgassing.**

2 **A. Parmigiani[1], W Degruyter[2], S. Leclaire[3.4], C. Huber[5] and O. Bachmann[1]**

3 [1]Institute of Geochemistry and Petrology, ETH Zurich, Clausiusstrasse 25, 8092 Zurich,
4 Switzerland.
5 [2]School of Earth and Ocean Sciences, Cardiff University, Main Building, Park Place, Cardiff,
6 CF10 3AT, Wales, UK
7 [3]Computer Science Department, University of Geneva, Route de Drize 7, 1227 Carouge,
8 Switzerland
9 [4]Department of Chemical Engineering, Polytechnique Montréal, 2500, Chemin de
10 Polytechnique, Montreal, H3T 1J4, Canada
11 [5]Department of Earth, Environmental and Planetary Sciences, Brown University, Rhode
12 Island 02912, USA
13

14 Corresponding author: Andrea Parmigiani (andrea.parmigiani@erdw.ethz.ch)

15 **Key Points:**

16 • Outgassing potential of a magma reservoir is a strong function of its crystal content.

17 • Outgassing efficiency is also modulated by mechanical coupling between reservoir
18   and crust.

19 • Simulations that consider both aspects reveal that the majority of exsolved volatiles is
20   released at intermediate to high crystallinity.
21

Abstract

Magma degassing fundamentally controls the Earth's volatile cycles. The large amount of gas expelled into the atmosphere during volcanic eruptions (i.e. volcanic outgassing) is the most obvious display of magmatic volatile release. However, owing to the large intrusive:extrusive ratio, and considering the paucity of volatiles left in intrusive rocks after final solidification, volcanic outgassing likely constitutes only a small fraction of the overall mass of magmatic volatiles released to the Earth's surface. Therefore, as most magmas stall on their way to the surface, outgassing of uneruptible, crystal-rich magma storage regions will play a dominant role in closing the balance of volatile element cycling between the mantle and the surface. We use a numerical approach to study the migration of a magmatic volatile phase (MVP) in crystal-rich magma bodies ("mush zones") at the pore-scale. Our results suggest that buoyancy driven outgassing is efficient over crystal volume fractions between 0.4 and 0.7 (for mm-sized crystals). We parameterize our pore-scale results for MVP migration in a thermo-mechanical magma reservoir model to study outgassing under dynamical conditions where cooling controls the evolution of the proportion of crystal, gas and melt phases and to investigate the role of the reservoir size and the temperature-dependent visco-elastic response of the crust on outgassing efficiency. We find that buoyancy-driven outgassing allows for a maximum of 40-50 % volatiles to leave the reservoir over the 0.4-0.7 crystal volume fractions, implying that a significant amount of outgassing must occur at high crystal content (>0.7) through veining and/or capillary fracturing.

Index Terms and Keywords (up to 5):

Magma reservoirs outgassing, gas migration in mushes, multiscale modeling of magma reservoirs, Earth's volatile cycle.

Introduction

On Earth, magmatic processes control the exchange of volatile species (H_2O, CO_2, S, Cl, F, Li, B, noble gases …) between the mantle and the atmosphere. The volatiles are initially dissolved in silicate melts produced in the upper mantle. As magmas ascend to shallower levels and undergo crystallization, a low viscosity and low density Magmatic Volatile Phase (hereafter MVP) can exsolve. The various processes that govern the transport and extraction of the MVP, as it leaves its shallow magmatic hearth and reaches the surface, remain a major challenge to our understanding of volatile cycling between the mantle and the surface.

Magma outgassing at shallow reservoir storage depth, here referred to as *intrusive outgassing*, is likely to be dominant over gas release through volcanic eruptions, here referred to as *volcanic outgassing*, as (1) plutonic rocks are typically dry (<1 wt.% H_2O when fully solid [*Caricchi and Blundy*, 2015; *Parmigiani et al.*, 2014; *Whitney*, 1988]), and (2) most of the magma stalls in the crust (intrusive:extrusive ratio between 10:1 and >30:1 in most arc settings [*Lipman and Bachmann*, 2015; *Ward et al.*, 2014; *White et al.*, 2006]). The amount of volatiles expelled during volcanic eruptions can be spectacular [*Iacovino et al.*, 2016; *Soden et al.*, 2002; *Vidal et al.*, 2016; *Westrich and Gerlach*, 1992], but is likely to constitute only a small fraction of the overall mass budget. *Shinohara* [2013] estimated a global budget of volatile release of volcanic centers in Japan over the last ~40 years to which explosive eruptions only contributed less than 15%, supporting the idea that volcanic eruptions do not provide the largest share of volatiles to the atmosphere at subduction zones. Hence, gaining insights into the physical and chemical processes regulating outgassing in shallow magma reservoirs is not only a crucial piece of the puzzle for constraining the state of magmas stalling in the Earth's crust [e.g., *Anderson et al.*, 1984; *Boudreau*, 2016; *Huber et al.*, 2010; *Mungall*, 2015; *Pistone et al.*, 2015; *Sisson and Bacon*, 1999], but it is also fundamental to volatile cycling and ore formation [*Candela*, 1991; *Chelle-Michou et al.*, 2017; *Gerlach*, 1991; *Heinrich and Candela*, 2012; *Huybers and Langmuir*, 2009; *Shinohara*, 2008; *Sillitoe*, 2010; *Wallace*, 2005; *Weis et al.*, 2012; *Zellmer et al.*, 2015].

Volatile exsolution is largely controlled by the pressure-temperature evolution of magmas in the crust. Magma reservoirs are known to build incrementally over time [*Annen et al.*, 2006; *Gelman et al.*, 2013; *Karakas and Dufek*, 2015; *Karakas et al.*, 2017; *Lipman*, 2007; *Menand et al.*, 2015; *Miller et al.*, 2011], and spend most of their supra-solidus life at high crystallinity (i.e. mush state [*Bachmann and Bergantz*, 2008; *Cooper and Kent*, 2014; *Huber et al.*, 2009; *Lee and Morton*, 2015; *Marsh*, 1981]). In arcs, magmas are commonly volatile-rich (i.e. > 4 wt.% H_2O [*Blundy et al.*, 2010; *Plank et al.*, 2013]) and are expected to reach a high volume fraction of MVP in mush zones in the upper crust (upon significant crystallization of mostly anhydrous phases). Such conditions set the stage for efficient MVP mobility through the upper part of the magmatic column [*Candela*, 1994; 1997; *Huber et al.*, 2010; *Parmigiani et al.*, 2014; *Parmigiani et al.*, 2016].

At high MVP and average crystal volume fractions, crystal confinement tends to favor MVP migration [*Huber et al.*, 2010; *Oppenheimer et al.*, 2015; *Parmigiani et al.*, 2011; *Parmigiani et al.*, 2016; *Spina et al.*, 2016] by promoting the formation of continuous and elongated MVP fingers, which serve as preferential outgassing pathways [*Parmigiani et al.*,

2014; *Parmigiani et al.*, 2016]. Additionally, an increase in melt segregation rate due to bubble growth ("gas filter-pressing" [*Pistone et al.*, 2015; *Sisson and Bacon*, 1999]), compaction, and melt buoyancy induced by a growing suspended MVP volume fraction [*Boudreau*, 2016], may favor the simultaneous physical segregation of melt and bubbles from the crystal-rich environment. This process may favor the extraction of eruptible high-SiO$_2$ rhyolite lenses and aplite-pegmatite bodies through an extended MVP-generated micro-fracture (veins) network [*Pistone et al.*, 2015; *Weinberg*, 1999].

In this study, we investigate shallow magma reservoir outgassing by coupling a pore-scale hydrodynamics study of MVP fingers formation to a magma reservoir scale model (Fig. 1). The pore-scale simulations focus on the competition between buoyancy and capillary stresses that takes place at the pore-scale and its effect on outgassing in rheologically-locked crystal-rich magma storage regions. We constrain the critical MVP volume fraction ε_g^{cr} that is needed for MVP migration by fingering to take place. These pore-scale simulations illustrate the complex multiphase fluid dynamics that govern the transport of MVP. As such, the pore-scale simulations provide an upper bound for the outgassing efficiency by considering that transport is the limiting factor. However, other thermo-mechanical feedbacks may control outgassing at the reservoir scale. Hence, we introduce the pore-scale results as a parameterization into a magma reservoir model to further test the impact of reservoir size, the temperature-dependent visco-elastic response of the surrounding crust on outgassing efficiency, as well as the effect of transient cooling and crystallization on gas exsolution and migration.

2. MVP mobility at the pore-scale: the competition between buoyancy and capillary stresses.

To model the MVP migration at the pore scale we make the following assumptions:

1. the timescale for MVP exsolution by crystallization ("second boiling") is longer than the time for the MVP to potentially establish flow pathways (if they occur),
2. pore-scale pressurization due to volatile exsolution is limited and likely efficiently dissipated through the permeable mush,
3. the crystal framework remains static (no deformation) over the time required for the MVP to migrate through the domain [*Parmigiani et al.*, 2016],
4. due to the limited vertical extent of our pore-scale sample volume (~ few cubic centimeters), the ambient (lithostatic) pressure is uniform,

123   5. although Fe-Ti oxides and sulfide phases are potential nucleation sites for bubbles
124   [*Edmonds et al.*, 2015; *Gardner and Denis*, 2004; *Navon and Lyakhovsky*, 1998], they
125   are by far volumetrically secondary to other non-wetting mineral phases such as
126   plagioclase. Therefore, we consider MVP as non-wetting [*Huber et al.*, 2010; *Huber et*
127   *al.*, 2012; *Parmigiani et al.*, 2014].

128   The mode of MVP transport discussed here will be referred to as hydrodynamic
129 migration (also known as "capillary invasion"), and it is expected to be efficient as long as the
130 effective permeability for the MVP does not allow for significant overpressure to build up
131 locally at the pore scale. Our pore-scale calculations focus on this regime. However, for large
132 crystal volume fraction (>~70 vol.%) and/or small average crystal size (lower pore-to-pore
133 connectivity), the capillary resistance to bubble migration will become significant. Hence, in
134 natural environments, local pressurization can potentially occur. Initially, such local
135 pressurization, together with bubbles hydrostatic pressure drop, can allow elongated bubbles
136 (or slugs) to overwhelm the capillary entry pressure of adjacent throats and drive bubble/slug
137 migration in a capillary invasion mode. However, when significant local pressurization builds
138 up, a second, brittle, mode of MVP migration can be expected in crystal-rich magmas,
139 referred to as "capillary fracturing" [*Holtzman et al.*, 2012; *Oppenheimer et al.*, 2015].
140 Contrary to capillary invasion, capillary fracturing implies that the bubble excess pressure
141 exceeds both the confining stress and the frictional resistance of the crystalline medium,
142 inducing matrix deformation, crystal displacement (i.e. frictional sliding) [*Shin and*
143 *Santamarina*, 2010] and eventually bubble migration.

144   In the present study, we assume the crystalline matrix in the mush to resist frictional
145 sliding. Crystal matrix deformation due to MVP displacement is therefore not taken into
146 account in our pore-scale calculations. This assumption is valid in crystal-rich magmas where
147 the crystal volume fraction is above the critical random packing threshold (i.e. for crystal
148 volume fraction ~0.4), especially if we assume the mush to be coarse-grained (mm-sized
149 crystals) and consider a high confining pressure P_c (~1-2.5 kbars). We estimate the crystal
150 size D_c for which the transition from capillary invasion to capillary fracturing would occur
151 using the scaling law $D_c \sim (\sigma/\mu_f)P_c^{(-1)}$ [as in *Eriksen et al.*, 2015; *Holtzman et al.*, 2012] where
152 σ and μ_f are the interfacial tension between the two immiscible fluids and the friction
153 coefficient between crystals, respectively. In this context, the throat size is a proxy for crystal
154 size since the throat size scales with both decreasing crystal size and/or increasing crystal
155 volume fraction. The interfacial tension between an H_2O-dominated MVP and melt is $\sigma =$
156 0.07-0.1 N/m [*Mangan and Sisson*, 2005]. To our knowledge, the friction coefficient in a

157   connected crystal framework remains poorly constrained; however, it is most likely not

158   negligible as crystals have angular shapes and rough surfaces, which promote interlocking.

159   Choosing $\mu_f \sim 0.2$ as a lower bound (i.e. steel balls particle-particle friction coefficient [*Li et*

160   *al.*, 2005]) and a confining pressure $P_c \sim 1\text{-}2.5$ kbars yields a D_c on the order of nanometers.

161   This scaling argument suggests that at intermediate crystal volume fraction (e.g. $0.4 < \varepsilon_x < 0.7$),

162   where pore-to-pore connectivity remains significant, MVP migration is within the regime of

163   capillary invasion. At higher crystal volume fraction, instead, when the pore-to-pore

164   connectivity is low (throat size on the order of nanometers), capillary fracturing under shallow

165   magmatic conditions can become the dominant mode for MVP transport. Recent laboratory

166   experiments of bubble growth in silicate crystal-rich magmas with ~100 micrometer average

167   crystal size seem to support the idea that fractures only occur at $\varepsilon_x > 0.75$ [*Pistone et al.*, 2015].

168

169   In the hydrodynamics migration regime, the competition between buoyancy and

170   capillary stresses on MVP bubbles can be described by the Bond number (Bo):

171

172
$$Bo = \frac{\Delta \rho g D^2}{\sigma}$$

173   where $\Delta \rho$ is the density difference between the melt and MVP bubbles, g is the acceleration

174   due to gravity, D the bubble diameter and σ the interfacial tension. We estimate Bo values to

175   lie between 0.1-1 for medium to coarse grained crystal mushes with an average crystal size of

176   ~3-5 mm [*Bachmann and Bergantz*, 2004], using $\sigma = 0.07$ N/m ($0.024 < \sigma < 0.1$ N/m, *Hammer*

177   [2004]) and $\Delta \rho = 2000$ kg/m^3. Because of slow exsolution and limited pressure build-up, we

178   assume the bubble diameter D to be equal to the average pore diameter D_{pc} of the crystalline

179   environment. Heterogeneity in the crystal size and shape can sensibly affect the packing,

180   making the estimation of D_{pc} for natural environments difficult [*Barker and Mehta*, 1992].

181   However, for the sake of our Bo estimates, we set the ratio between pore diameter and grain

182   diameter to that found in randomly packed beds of spheres (0.2-0.4 at the random packing

183   threshold value) [*Barker and Mehta*, 1992; *Hinedi et al.*, 1997]; when using an average crystal

184   size of 3-5 mm, D_{pc} is therefore in the range ~0.6-2 mm.

185

186   We investigate MVP transport at the pore-scale by performing immiscible two-phase

187   lattice Boltzmann (LB) simulations (see pore-scale inset in Fig. 1 and Appendix A for more

188   information about the LB algorithm adopted for our investigation). We conduct our

189   simulations in rigid crystalline matrices with variable crystal volume fractions (see Fig. 2).

190   The size of the crystalline domain is set to 160x160x240 grid points. Crystal sizes vary

191   between ~10 and ~30 grid points. We first compute the intrinsic permeability of each medium

192   with a single fluid transport model (e.g. Fig. 2e-f) [*Degruyter et al.*, 2010] and, scale up the

193   results considering an average crystal size of 4 mm [*Cheadle et al.*, 2004] (see Fig. 2g).

194   Our simulation domains have periodic boundary conditions in all spatial directions and

195   no-slip internal boundary conditions (bounce-back scheme [*Chopard et al.*, 2002]) on the

196   crystal surfaces. The pore space is occupied by either a low density, low viscosity non-wetting

197   fluid or a more viscous wetting fluid, which represent the MVP and melt phase, respectively.

198   The MVP is fully non-wetting (contact angle 180°), where the wettability is set following the

199   approach of *Leclaire et al.*, 2016. The viscosity ratio between the melt and the MVP is set to

200   100, which is well under the real value but large enough to reproduce the correct stress

201   balance on bubbles [*Parmigiani et al.*, 2016]. The Reynolds number of our pore-scale

202   calculation is small for both early stages (i.e. while bubbles interacts to form channels Re < 1)

203   and MVP transport through channels (Re ~ 1). In our pore-scale simulations, various values

204   for the Bond number are set by varying the magnitude of the buoyancy force acting on the

205   vapor phase [*Ngachin et al.*, 2015; *Parmigiani et al.*, 2011; *Ren et al.*, 2016].

206   In order to mimic the initial spatial distribution of MVP associated with second

207   boiling, we distribute MVP bubbles with different radii randomly inside the crystalline matrix

208   (Fig. 3). The whole set of parameters explored with our calculations is reported in Appendix

209   A, Table 1. During the early stages of each simulation, bubbles sitting next to each other (e.g.

210   in the same pore or very well connected pores) can coalesce and form larger bubbles; this

211   occurs in particular at high bubble and crystal volume fractions (see Fig. 3).

212

213   **3. Results**

214   **3.1. Window of optimal outgassing efficiency**

215   We seek to determine the MVP volume fraction (ε_g) threshold at which connected

216   MVP channels can form (Fig.4a-b). Above the threshold, outgassing will be efficient, as it

217   significantly decreases the rate of energy dissipation during MVP migration [*Parmigiani et

218   al.*, 2016] (see Fig.4c and Fig.4d). We study the onset of dynamic MVP percolation over a

219   range of MVP (ε_g) and crystal (ε_x) volume fractions (i.e. $0.03 \leq \varepsilon_g \leq 0.19$ and $0.4 \leq \varepsilon_x$

220   ≤ 0.75) that are characteristic of isobaric (at ~2 kbars) degassing for intermediate arc magmas

221   (with ~4-7 wt.% H_2O). The dashed lines in Fig. 4e&f are MVP volume fraction for closed-

222   system degassing calculated with *rhyolite-MELTS [Gualda et al., 2012]*. We also consider

223   three Bo number values (Bo=0.1, 0.5, 1) to estimate the effect of the crystal/pore sizes on the

224   capillary resistive stresses exerted by the crystalline environment on bubble mobility.

225   Our results demonstrate that the competition between the positive effect of crystal

226   confinement on MVP channel formation and the capillary resistance to bubble mobility

227   controls the critical MVP volume fraction ε_g^{cr} at which fingering pathways of MVP form and

228   sustain. ε_g^{cr} is therefore a function of the crystal volume fraction ε_x (see Fig. 4e&f). The first

229   effect, crystal confinement, promotes more efficient outgassing by enhancing bubble

230   coalescence, deformation and migration, which ultimately favor channel formation and

231   stability [*Parmigiani et al.*, 2016]. The effect of crystal confinement on MVP migration is

232   clearly observed in Fig. 4b where it results in a negative $\partial\varepsilon_g^{cr}/\partial\varepsilon_x$ (Fig. 4e for Bo=0.5) up to

233    $\varepsilon_x \simeq 0.5$. For larger crystal volume fractions ($\varepsilon_x > 0.5$), $\partial\varepsilon_g^{cr}/\partial\varepsilon_x$ becomes positive and is

234   associated with the increasing capillary resistance to MVP migration as the mean pore throat

235   diameter decreases. At high crystallinity ($\varepsilon_x > 0.6$ for Bo=0.5 and $\varepsilon_x > 0.7$ for Bo=1), we observe

236   a shift in behavior, with MVP migration by fingering becoming inefficient (Fig. 4e&f). This

237   effect is enhanced when the crystal size is small ($\varepsilon_x > 0.5$ at Bo=0.1, Fig. 4f) and/or the crystal

238   content becomes very high (as shown by the positive correlation between ε_g^{cr} and ε_x in Fig.

239   4e&f).

240   Overall, we find a favorable crystallinity window (between $0.4 \leq \varepsilon_x \leq 0.7$ over

241    $0.1 \leq$ Bo≤ 1), where the combination of crystal confinement and limited capillary resistance

242   allows for MVP channel formation and optimal MVP migration. Our results suggest that at

243   Bo=0.5 and $\varepsilon_x > 0.7$, connected MVP channels do not form unless almost half of the pore-space

244   is occupied by MVP, conditions that have been suggested to be favorable to the formation of

245   percolation pathways strictly based on static-geometrical percolations arguments [*Candela*,

246   1994]. However, our calculations show that the strong non-wettability of the MVP impedes

247   the formation of percolating pathways unless bubbles are able to overcome the capillary

248   resistivity of the porous medium (bottlenecks in throats). We generally find that for $\varepsilon_x > 0.7$

249   and/or Bo<1, additional processes such as pore-pressure build-up by compaction [*Boudreau*,

250   2016] or bubble overpressure are required to initiate bubble migration, and eventually, when

251   pore connectivity is strongly reduced, by capillary fracturing [*Holtzman et al.*, 2012].

252   The formation and destruction of MVP channels control outgassing in crystallizing

253   magma bodies. MVP transport through channels is likely to be intermittent in magmatic

254   environments [*Candela*, 1994] since, in order to be stable, channels require an adequate

255   volatile flux [*Stöhr and Khalili*, 2006] that a magmatic source can sustain only for a limited

256　time [*Candela*, 1994; 1997]. Therefore, MVP channels are bound to pinch off, stopping

257　efficient outgassing, and leaving behind a trail of capillary trapped bubbles or slow moving

258　MVP fingers (MVP residual saturation). Such capillary-trapped bubbles will however

259　participate to the formation of new channels if additional MVP is injected or exsolved into the

260　system.

261

3.2. 2nd boiling vs. injection from below.

263　　　　The critical MVP volume fraction for MVP channel formation ε_g^{cr} (deduced from our

264　pore-scale simulations) depends on the mode of volatile delivery to the crystalline mush zone.

265　When the MVP is injected from below (Fig. 5a), as would be expected if a deeper section of

266　the magmatic system is undergoing significant degassing [*Parmigiani et al.*, 2014], ε_g^{cr} is a

267　monotonous function of ε_x and decreases with ε_x as would be expected for 2-phase percolation

268　governed by crystal confinement (Fig. 5b). In contrast, simulations initiated with a random

269　spatial distribution of bubbles (2nd boiling) require more MVP to reach a similar degree of

270　outgassing (Fig. 6-7). This difference is due to the MVP invasion process selecting only the

271　most efficient flow pathways in the scenario with MVP injection from below. In contrast, the

272　random distribution of MVP during 2nd boiling leads to a significant fraction of bubbles

273　trapped in poorly connected pores, which do not contribute to the overall MVP flux. The

274　difference in critical MVP volume fraction between 2nd boiling and injection from below

275　provides, therefore, a way to quantify the volume of MVP that remains trapped in the porous

276　medium after 2nd boiling until other processes such as capillary fracturing [*Holtzman et al.*,

277　2012] or gas-filter pressing [*Pistone et al.*, 2015] take place.

278

3.3 Outgassing parameterization

280　　　　We now wish to describe the efficiency of outgassing at the spatial and temporal

281　scales of the magma reservoir and test the effect of thermomechanical processes on

282　outgassing dynamics. To this end, we will couple the results of the pore-scale simulations

283　with a reservoir scale model using a parametrized approach. We build a pore-scale

284　parameterization for Bo=0.5 that describes MVP channel formation and enhanced outgassing

285　by estimating (1) the critical MVP volume fraction needed for channel formation (from Fig.

286　4e) and, once channels are formed, (2) the intrinsic (single-phase) permeability k of the

287　porous medium (Fig. 2g), and (3) the MVP relative permeability of the mush k_r (Fig. 8). We

288　retrieve the relative permeability for the MVP by calculating the MVP discharge through the

289　crystalline medium (Fig. 8).

290   Although our results also indicate an increase in relative permeability with increasing

291 MVP volume fraction (for $\varepsilon_g > \varepsilon_g^{cr}$), reflecting the ability to form more than one connected

292 MVP finger through the porous network or improving MVP channels connectivity, only k_r

293 estimated at the onset of MVP channel formation for each explored crystal volume fraction is

294 used for the parameterization. When migration becomes efficient with respect to exsolution,

295 the MVP volume fraction is bound to remain close to ε_g^{cr}. Due to the positive effect of solid

296 confinement on MVP channel formation and outgassing, we observe a non-linear increase in

297 MVP discharge and relative permeability with increasing crystal volume fraction, with a

298 maximum value around ε_x=0.5. We find that the MVP discharge can vary by three orders of

299 magnitude between 0.4<ε_x<0.7.

300   For Bo=0.5 and crystal volume fraction between 0.4 and 0.7, our pore scale

301 simulations yield the following relationship between the critical MVP volume fraction and the

302 crystal volume fraction (Fig. 4e-f):

303    $$\varepsilon_g^{cr} = 2.75\varepsilon_X^3 - 2.79\varepsilon_X^2 + 0.6345\varepsilon_X + 0.0997 \qquad (1).$$

304 Similarly, we find the following correlation between the intrinsic permeability and the crystal

305 volume fraction:

306    $$k = 10^{-4}(-0.0534\varepsilon_X^3 - 0.1083\varepsilon_X^2 - 0.0747\varepsilon_X + 0.0176)\ m^2 \qquad (2).$$

307 Finally, our calculations lead to the following expression for the relative permeability as a

308 function of the crystal volume fraction:

309    $$k_r = -2.1778\varepsilon_X^4 + 5.1511\varepsilon_X^3 - 4.5199\varepsilon_X^2 + 1.7385\varepsilon_X - 0.2461 \qquad (3).$$

310

311

312

313 **4. Coupling the pore-scale dynamics with a large-scale thermo-mechanical magma**

314 **reservoir model**

315   We implement the pore MVP migration parameterization of Eqs 1-3 (see Fig. 9) in a

316 reservoir-scale model [*Degruyter and Huber*, 2014; *Degruyter et al.*, 2016] to provide

317 quantitative estimates of the proportion of volatiles exiting the reservoir over various ranges

318 of crystal content during the cooling of a shallow magma reservoir. Our goal is to assess the

319 importance of factors that cannot be considered explicitly in the pore-scale simulations (e.g.,

320 reservoir size, temperature and rheology of the wall-rocks) as well as transient cooling, which

321 controls the temporal evolution of the relative proportions of the three phases in the magma

322 reservoir (melt, crystals and exsolved volatiles).

323   The thermo-mechanical evolution of the magma reservoir is solved with a lumped

324   parameter approach (see Appendix B). We consider an initially mobile (crystal volume

325   fraction <0.4) 3-phase magma volume, which we refer to as the magma chamber, that sits in a

326   colder visco-elastic shell (a crystal mush that gradually transitions into the surrounding crust).

327   The magma chamber is considered homogeneous, which allows tracking the evolution of the

328   average volume fraction and density of the melt, crystals and MVP. The different phases are

329   assumed to be in equilibrium. We further track the changes in pressure, temperature, and

330   volume of the magma chamber. For this study, we consider the scenario of a monotonously

331   cooling magma chamber at 2 kbar that crystallizes and exsolves a MVP and 2nd boiling is

332   therefore the only source of MVP.

333   Natural subvolcanic magma reservoirs are likely to be not as homogeneous as

334   assumed in our model. Heterogeneities (particularly in crystal content (see Fig. 1); e.g.,

335   *Bachmann and Bergantz* [2004]; *Gutierrez et al.* [2013]; *Hildreth* [2004]; *Marsh* [1989]) may

336   influence channels formation, either enhancing (in the most crystalline parts) or decreasing (in

337   crystal-poor regions) MVP bubbles connectivity [*Parmigiani et al.*, 2016]). However, we note

338   that magmas are likely to be dominantly stored as fairly homogeneous crystal mushes [*Huber

339   et al.*, 2009], and the volumes of crystal-poor regions, potentially storing volatiles (decreasing

340   outgassing), are limited with respect to the overall bulk mush; therefore, the outgassing

341   efficiency predicted by our volume-averaged approach should be relatively robust.

342

343   **5. Thermo-mechanical reservoir model: results**

344   We performed two sets of magma reservoir simulations to focus on the effects of (1)

345   temperature dependent rheology of the crust (visco-elastic crust with a far-field temperature

346   of 250 and 300 °C, respectively) and (2) the size of the chamber, on outgassing (initial size of

347   the chamber from 5-500 km^3). The temporal evolution of the crystal content for each of these

348   simulations is reported in Fig.10, where time is normalized by the cooling time scale τ_c=

349   R^2/ κ, with R the initial radius of the reservoir and κ the thermal diffusivity of the crust (Table

350   2). Since the crystal content for each of the two tested scenarios follows a very similar

351   temporal trend (Fig.11 & 12), we can describe (1) the total volatile mass fraction evolution,

352   (2) the volatile mass fraction loss, (3) the overpressure of the reservoir and (4) the MVP

353   volume fraction evolution as a function of crystal volume fraction.

354   We find that outgassing is limited by the availability of MVP (as in the pore-scale

355   simulations, i.e., saturation-limited) in large magma reservoirs hosted within a hot and

356   compliant crust (Fig. 1 (a); Fig. 11 & Fig. 12). This is because the decompression of the

357 reservoir caused by the loss of MVP is damped by the viscous relaxation of the surrounding

358 crust; the pressure in the reservoir therefore remains near lithostatic and prevents the

359 development of significant adverse pressure gradients that would impede outgassing. A colder

360 crust and/or smaller reservoir, on the other hand (Fig.1 (b); Fig.11 & Fig.12), responds mostly

361 elastically to the volume loss associated with outgassing, which mechanically hinders the

362 efficiency of the outgassing process as pressure gradients oppose the migration of the MVP

363 out of the reservoir.

364 A hot crust and large reservoir are most favorable for outgassing. Under these

365 conditions, our model shows that the magma with an initial water content of 5.5 wt.% can lose

366 up to ~40 % of its original water content before reaching $\varepsilon_x \cong 0.7$ (total water content after

367 outgassing from MVP channels decreases to 3.25 wt.%, see Fig. 11a&c). Such value is clearly

368 dependent on the choice of Bo number value (here Bo=0.5), initial water content (here 5.5

369 wt.% H2O), and reservoir depth (2 kbars ~ 8-10 km depth). Higher initial water content,

370 shallower storage levels and larger crystal/pore sizes would enhance the amount of water

371 released before the capillary fracturing stage.

372 Nonetheless, our calculations show that a substantial amount of volatiles remain

373 trapped by capillary forces above ε_x>0.7. As plutons have a residual volatile content typically

374 <1 wt.% [*Caricchi and Blundy*, 2015; *Whitney*, 1988], the remaining MVP must ultimately

375 escape the cooling reservoirs by alternative processes such as gas-filter pressing [*Pistone et*

376 *al.*, 2015; *Sisson and Bacon*, 1999] and capillary fracturing [*Holtzman et al.*, 2012; *Shin and*

377 *Santamarina*, 2010] that are not taken into account into our pore-scale parametrization. These

378 processes likely enhance the extraction of the melt-MVP mixture and lead to the generation of

379 either eruptible high SiO_2 melt pockets [*Bachmann and Bergantz*, 2003] or aplite and

380 pegmatite veins [*London and Morgan*, 2012; *Thomas and Davidson*, 2013].

381 Therefore, in light of our reservoir scale simulations, we suggest that intrusive

382 outgassing occurs via three stages controlled by different processes:

383 1. by discrete (non-connected) bubbles (ε_x≤0.4) that roughly accounts for a few % of

384 the total amount of MVP outgassed;

385 2. by permeable outgassing via MVP channel formation (0.4≤ε_x≤0.7) that contributes

386 to about 40-50% of the outgassing, and,

387 3. by capillary fracturing (ε_x>0.7), for the remaining of MVP loss.

388

389 The differences in style and rates between outgassing at low and high crystallinity will

390 control the mass flux and composition of the magmatic gases released to the Earth's surface.

391   For instance, volatile species with a low solubility, or high compatibility with the MVP (e.g.,

392   S, Ar, N_2) are likely to partition into the MVP at low crystallinity and outgas predominantly

393   during spikes of volcanic activity [*Shinohara*, 2013]. In contrast, less water-compatible or

394   more soluble species (F, Br, and to some extent He) are expected to be dominantly released

395   passively from intrusive bodies ("mush zones"; [e.g. *Paonita*, 2005]).

396   **6. Conclusion**

397   The multiscale modeling approach presented here allows us to shed light on the

398   physical processes that control MVP outgassing in shallow silicic magmatic reservoirs. Our

399   pore-scale numerical experiments at different Bond numbers (Bo=0.1-1 for mm-sized

400   crystals), MVP and crystal volume fractions highlight the presence of a favorable crystal

401   volume fraction window (0.4-0.7) where the buoyant MVP phase can overcome capillary

402   forces and form MVP channels. We determine the critical MVP volume fraction for MVP

403   channels to form as a function of crystal volume fraction. The pore-scale mechanics of bubble

404   migration is then introduced as a parameterization in a thermo-mechanical magma reservoir

405   model, which allows us (1) to compare directly outgassing efficiency over different ranges of

406   crystal content in an evolving environment and (2) to constrain the role of the rheology of the

407   surrounding crust on the mass balance of exsolved volatiles in the reservoir. This multiscale

408   approach reveals that the size of the reservoir and visco-elastic response of the crust that

409   surrounds it play a major role in the efficiency of intrusive outgassing. Large reservoirs and a

410   hot crust (i.e. more prone to accommodate differential stresses viscously) allow for more

411   substantial outgassing before the onset of capillary fracturing. Small reservoirs and/or colder

412   crust (i.e. elastic stress response) are more prone to develop an adverse pressure gradient that

413   favors a late-stage capillary fracturing mode of outgassing.

414   Under favorable conditions (viscous relaxation of the crust, Bo=0.5 and lithostatic

415   pressure of 2 kbar), our simulations show that up to 40% of the initial water content of the

416   magma can be released through MVP outgassing through MVP channels formation. Hence,

417   other outgassing processes are needed to explain the very low residual water content of

418   plutonic rocks in arcs. We suggest that at high crystal volume fraction (>0.7), ductile veining

419   [*Weinberg and Regenauer-Lieb*, 2010] or capillary fracturing [*Holtzman et al.*, 2012;

420   *Oppenheimer et al.*, 2015; *Shin and Santamarina*, 2010] may be viable process for MVP

421   outgassing when magmas approach their solidus.

422

423   **Appendix A. Lattice Boltzmann calculations**

424 The lattice Boltzmann method (LBM) is a computational fluid dynamics technique that solves

425 a discrete version of the Boltzmann equation [*Chopard et al.*, 2002]. LBM is well suited for

426 dealing with complex multiphase fluids, and can be conveniently parallelized. These features

427 allow LBM to be particularly efficient in modeling immiscible multiphase fluid flows in

428 porous media [*Huber et al.*, 2013]. In order to take advantage of the parallel efficiency of

429 LBM, we implemented the algorithm in an open-source parallel solver for LBM, Palabos

430 (www.palabos.org) and performed our calculations on large computer cluster facilities (Dora

431 at CSCS and Euler at ETHZ).

432

433 We perform our isothermal two-phase fluid flow pore-scale calculations with the color-

434 gradient model (CGM) and a single relaxation time collision scheme that is based on *Leclaire*

435 *et al.*, 2017. This CGM model allows us to deal with high viscosity ratios between the two

436 immiscible fluids and explore a wider range of physical parameters compared to other lattice

437 Boltzmann multiphase solvers [*Liu et al.*, 2016]. The CGM is well suited to deal with the

438 competition between capillary, buoyancy and viscous stresses. This method was extensively

439 tested against various benchmarks [*Leclaire et al.*, 2012].

440

441 The core algorithm of the color-gradient method is divided in six computational steps that are

442 repeated at each time increment. We use the D3Q15 lattice since this cubic three-dimensional

443 lattice offer the smallest computational workload [*Leclaire et al.*, 2017]. The probability

444 distribution functions (PDFs) $N_i^k(\mathbf{x}, t)$ and the indices $i=(0,1,\ldots13,14)$ and k are respectively

445 related to the velocity space discretization and the "color" of the fluid (e.g. $k=r$ for a red fluid

446 and $k=b$ for a blue fluid; for this manuscript, the red fluid is the MVP non-wetting phase

447 (used index g), while blue one is the melt wetting phase (used index m)) describe the

448 probability of finding a particle of fluid color k at position $\mathbf{x}$ and time t. In the CGM, the

449 color-blind distribution function is important and for two-phase flow it is defined as

450
$$N_i(\mathbf{x}, t) = N_i^r(\mathbf{x}, t) + N_i^b(\mathbf{x}, t) \qquad\qquad \text{A.1}$$

451 The first step consists of the color-blind single-relaxation-time lattice Boltzmann collision:

452
$$N_i^* = N_i - \omega_{eff}(N_i - N_i^e) + \Delta N_i \qquad\qquad \text{A.2}$$

453 where N_i^* is the distribution functions after the single-phase collision step. The quantity

454 $\omega_{eff} = \frac{2}{6\nu+1}$ is the relaxation factor and is related to the effective kinematic viscosity of the

455 fluids $\nu(\mathbf{x}, t) = \frac{\rho_r(x,t)\nu_r + \rho_b(x,t)\nu_b}{\rho_r(x,t) + \rho_b(x,t)}$, a density-weighted interpolation applied at the interface

456 between the fluids to handle the desired viscosity contrast. ρ_k and $\nu_k = (1/3)(\tau_k - 0.5)$ are

457 the density and kinematic viscosity for fluid k respectively; τ_k is the relaxation time for fluid

458 k. The details of the equilibrium function N_i^e are given in *Leclaire et al.*, 2017, but essentially

459 they depend on the local density $\rho_k(x,t)$ and velocity of the fluid $\mathbf{u}(x,t)$ as well as on the non-

460 local color-blind density gradient $\nabla\rho(\mathbf{x},t)$. The local density and velocity of each fluid are

461 obtained from the first and second moments of the distribution functions. The term ΔN_i

462 allows us to add external forces, such as buoyancy force. The buoyancy of the MVP is

463 introduced with $\Delta N_i = \text{Bo} \, (\sigma_{lu} / D_{lu}^2) \, \boldsymbol{c}_{i,z}$ applied to the non-wetting fluid only [*Parmigiani et*

464 *al.*, 2011], where Bo is the Bond number, σ_{lu} is the surface tension and D_{lu} the average

465 diameter of the pore of the crystalline medium in lattice units (l.u) (see table 2).

466

467 The second step allows us to enforce the proper wetting conditions. Since the buoyant phase

468 (MVP) is modeled as fully non-wetting, we can use the standard wetting boundary condition

469 which uses ghost nodes and fictive density. This is done following the approach of *Leclaire et*

470 *al.*, 2016.

471

472 The third step of the color-gradient method introduces interfacial tension effects at the

473 interfaces between the immiscible fluids using a perturbation operator:

$$N_i^{**} = N_i^* + A|\mathbf{F}| \left(w_i \, \frac{(\mathbf{F}\cdot\boldsymbol{c}_i)^2}{|\mathbf{F}|^2} - B_i \right) \qquad \text{A.3}$$

475 where the constant A is related to the strength of the interfacial force, and the weights w_i and

476 B_i are lattice dependent weights [*Leclaire et al.*, 2017]. At last, the color gradient $\mathbf{F}$ is an

477 approximation to the normal of the fluid-fluid interface:

$$\mathbf{F} = \nabla \left(\frac{\rho_r - \rho_b}{\rho_r + \rho_b} \right) \qquad \text{A.4}$$

479 The perturbation operator introduces the capillary stress tensor back into the equations for

480 immiscible two-phase flows [*Reis and Phillips*, 2007].

481

482 The fourth step is a recoloring operation, which is designed to preserve immiscibility while

483 respecting mass and momentum conservation laws as well as controlling exactly the finite

484 width of the interface [*Leclaire et al.*, 2015]:

$$N_i^{r,***} = \frac{\rho_r}{\rho} N_i^{**} + \beta \frac{\rho_r \rho_b}{\rho^2} \cos(\varphi_i) N_i^e (\rho, \mathbf{0}) \qquad \text{A.5}$$

$$N_i^{b,***} = \frac{\rho_b}{\rho} N_i^{**} - \beta \frac{\rho_r \rho_b}{\rho^2} \cos(\varphi_i) N_i^e (\rho, \mathbf{0}) \qquad \text{A.6}$$

487 where β is a parameter controlling the thickness of the numerical interface. In this study, we

488 set $\beta = 0.7$ (see Table 1) for an optimal trade-off of the interface thickness between the two

489   immiscible fluids and the magnitude of the spurious velocities. The φ_i is the angle between

490   the color gradient $\mathbf{F}$ and the lattice connectivity vector $\mathbf{c}_i$.

491

492   The fifth step is related to the solid-fluid boundary conditions for the distribution functions.

493   The model we use here includes a solid-fluid no-slip boundary condition with the full-way

494   bounce back approach [*Chopard et al.*, 2002], and finally, the sixth and last step is the usual

495   lattice Boltzmann streaming step for each colored fluid.

496

497   **Appendix B. Lumped parameter model for magma reservoir**

498   The reservoir model of Degruyter and Huber [2014] solves the conservation of total

499   mass (melt + crystals + volatiles), the conservation of water (most abundant magmatic volatile

500   component), and enthalpy. The governing equations of the magma chamber model can be

501   written in a condensed form as

502     $$\frac{dM}{dt} = \dot{M}_{in} - \dot{M}_{out} \quad \text{(conservation of mass),} \tag{B.1}$$

503     $$\frac{dM^w}{dt} = \dot{M}_{in}^w - \dot{M}_{out}^w \quad \text{(conservation of water),} \tag{B.2}$$

504     $$\frac{dH}{dt} = \dot{H}_{in} - \dot{H}_{out} \quad \text{(conservation of enthalpy),} \tag{B.3}$$

505   with M, M^w, and H the (total) mass, the water mass and the enthalpy of the magma chamber,

506   respectively. The index "*in*" refers to source terms, while "*out*" indicates sink terms. We do

507   not consider the injection of new magma and all the inflow terms are set to zero. There is also

508   no mass loss due to eruptions and therefore the loss of mass reduces to outgassing $\dot{M}_{out} =$

509     $\dot{M}_{out}^w = \dot{M}_{og}$ (the index "*og*" refers to MVP outgassing). The heat loss term $\dot{H}_{out} = \dot{Q}_{out} +$

510     $\dot{H}_{pd}$, where $\dot{Q}_{out}$ represents the heat flow out of the magma chamber into the colder

511   surrounding shell. This term is calculated using an analytical solution of an evolving

512   temperature profile between a spherical magma chamber and a larger spherical shell with a

513   radius ten times the initial radius of the magma chamber. The temperature of the outer shell is

514   constant and set to the far-field temperature expected at the depth of the chamber (Table 2).

515   The rheology of the surrounding shell is calculated according to the approach of *Dragoni and*

516   *Magnanensi* [1989] and its effective viscosity is determined by the temperature profile in the

517   crust. We thus can test the effect of crustal rheology on outgassing by varying the temperature

518   at the boundary of the outer shell (Table 2). The mass and enthalpy loss rates during

519   outgassing, ($\dot{M}_{og} = \rho_g \varepsilon_g U_{og} S$ and $\dot{H}_{og} = c_g T \dot{M}_{og}$) are calculated as follows:

520   • the MVP density ρ_g and the MVP volume fraction ε_g are obtained from the

521   model,

522   •   the surface area S is a constant in our calculations and is set to be a circular
523   cross-section with a radius equal to the initial radius of the magma chamber,

524   •   the MVP specific heat c_g is set to 3900 K/kg/K, [*Huber et al.*, 2010; *Lemmon et*
525   *al.*, 2003]) and T is the average magma chamber temperature obtained from the
526   model.

527   •   the outgassing volume flux U_{og} is defined through closure expressions that we
528   vary as a function of crystal and MVP volume fractions according to the results
529   of the pore-scale simulations discussed in the main text.

530 For this, we divide the $(\varepsilon_m, \varepsilon_x, \varepsilon_g)$-space into four regions (Fig. 9), according to
531 different possible outgassing mechanisms:

532   • $\varepsilon_g > 0.5$ (white region in Fig. 9): the MVP phase is the carrier phase. This condition is
533   unlikely to be reached for realistic amounts of water at common storage depths.
534   However, it can become relevant for magma ascent and fragmentation during
535   explosive eruptions, which is beyond the scope of this study. The volume flux is not
536   defined for this region.

537   •   If $\varepsilon_g \leq 0.5$ and $\varepsilon_x < 0.4$ (blue region in Fig. 9): the MVP ascends as individual bubbles.
538   The melt is the carrier phase and crystals cannot yet support a load. The volume flux
539   U_{pd} is based on Stokes law for the ascent of an individual MVP bubble in a suspension
540   [*Faroughi and Huber*, 2015; *Faroughi and Huber*, 2016]:

$$U_{og} = \frac{U^*(\rho_m - \rho_g)gr_b^2}{3\mu_{mx}} \qquad \text{B.4}$$

542 with ρ_m, ρ_g the density of the melt and MVP phase calculated in the model; $g = 9.81$
543 m/s^2 the gravitational acceleration; $r_b = 100$ μm is the bubble radius; U^* the hindrance
544 function related to the gas volume fraction ε_g:

$$U^* = \left(\frac{1-\varepsilon_g}{1-\frac{1}{2}\left(\frac{\varepsilon_g}{\psi_m}\right)}\right)\left(\frac{\psi_m - \varepsilon_g}{\psi_m(1-\varepsilon_g)}\right)^{\left(\frac{\psi_m}{1-\psi_m}\right)}\left(1 - \Upsilon\left(\frac{\varepsilon_g}{\psi_m}\right)^{\frac{1}{3}}\right) \qquad \text{B.5}$$

546 with $\psi_m = 0.637$ the maximum random close packing fraction for mono-sized spherical
547 particles and $\Upsilon = 0.45$ a geometrical constant derived from best fit value of
548 experimental data for particles and drop suspensions experiments; μ_{mx} is the viscosity
549 of the melt-crystal mixture:

$$\mu_{mx} = \mu_m \mu^* \qquad \text{B.6}$$

551 with μ^* the hindrance function related to crystal volume fraction ε_x:

$$\mu^* = \left(\frac{\psi_m - \varepsilon_X}{\psi_m(1-\varepsilon_X)}\right)^{-2.5\left(\frac{\psi_m}{1-\psi_m}\right)}, \qquad \text{B.7}$$

553   where μ_m is the viscosity of the melt is calculated using the parameterization of *Hess*

554   *and Dingwell* [1996] for silicic melts:

555
$$\log_{10} \mu_m = [-3.545 + 0.833 \ln(100 m_{eq})] + \frac{[9601 - 2368 \ln(100 m_{eq})]}{[T - [195.7 + 32.35 \ln(100 m_{eq})]]}, \qquad \text{B.8}$$

556   where m_{eq} is the dissolved water content in the melt and T the average temperature of

557   the magma chamber (both evolving in the model).

- If $\varepsilon_g \leq 0.5$, $0.4 \leq \varepsilon_x < 0.7$, and $\varepsilon_g \geq \varepsilon_g^{cr}$ (black region in Fig. 9; equation (1)): outgassing

559   can occur through connected MVP channels in a rigid crystal mush. The volume flux

560   here is governed by a multiphase Darcy's law [*Paonita et al.*, 2016; *Weis et al.*, 2012]:

561
$$U_{og} = f_s \frac{k_r k}{\mu_g} \left(\frac{P - P_{lit}}{L} + (\rho_m - \rho_g) g \right) \qquad \text{B.9}$$

562   where the first term on the right hand side represents pressure driven flow with P the

563   pressure of the magma body; P_{lit} is the lithostatic pressure set at 2 kbar; L is a

564   characteristic length scale for the pressure-driven flow set to 100 m (which is

565   equivalent to having a maximum under-pressure of a couple of MPa). The second term

566   is the buoyancy force with ρ_m, ρ_g the density of the melt and gas phase and $g = 9.81$

567   m/s^2 the gravitational acceleration. k_r is the relative permeability defined in equation

568   (3); k is the intrinsic permeability defined in equation (2), and the gas viscosity is set

569   to $\mu_g = 6e^{-5}$ Pa s [*Lemmon et al.*, 2003]. f_s is an additional smoothing function to

570   assure numerical stability across different outgassing regions:

571
$$\text{If } \varepsilon_g < \varepsilon_g^{cr} + 0.04, f_s = \left((\varepsilon_g - \varepsilon_g^{cr})/0.04 \right)^4, \qquad \text{B.10}$$

572   else, $f_s = 1$.

- If $\varepsilon_x \geq 0.4$, and $\varepsilon_g < \varepsilon_g^{cr}$ (green region in Fig. 9; equation (1)): outgassing stops and U_{og}

574       $= 0$ because there is not enough MVP to form/stabilize connected pathways. Bubbles

575   remain trapped in the mush, and other processes such as capillary fracturing are

576   necessary to promote further outgassing.

577   This set of equations closes the governing equations, which we solve using the ode15s

578 subroutine in Matlab [*Shampine and Reichelt*, 1997], which is particularly well suited for stiff

579 ordinary differential equations. We performed several reservoir calculations using the

580 parameters and initial conditions reported in Table 2. The initial volume was varied to test the

581 effect of a changing reservoir size on outgassing efficiency. All other model parameters are

582 set to default values defined in *Degruyter and Huber* [2014].

583

584 **Acknowledgements**

599

600 **FIGURES CAPTION:**

601 **Fig.1: Schematic representation of modelling approach for outgassing shallow reservoir**

602 **(modified from Bachmann and Huber, 2016).** We use a multiscale numerical approach to

603 study the physics of outgassing in shallow magma reservoirs. At the pore-scale, we

604 investigate the hydrodynamic conditions that allow MVP fingers to form by using a numerical

605 isothermal pore-scale model for two-phase immiscible flows based on the lattice Boltzmann

606 (LB) method. MVP bubbles (red) migrate because of their hydrostatic pressure drop (bubbles

607 are buoyant) in a crystalline rigid environment (gray), coalesce and possibly form MVP

608 fingers. Pore-scale results are then inserted as a parameterization into a thermomechanical

609 magma reservoir model to provide a holistic view of the gas migration in cooling magma

610 reservoirs.

611 **Fig.2: Synthetic crystal-matrices and intrinsic permeability. a-d**: Matrices at different

612 crystal volume fractions produced with a crystal nucleation and growth algorithm similar to

613 Avrami [1939] and modified by Hersum and Marsh [2006] that were used for our pore-scale

614 calculations (size 160x160x240 l.u.). **e&f**: single fluid flow velocity field through crystalline

615 matrix with $\varepsilon_x=0.6$ and $\varepsilon_x=0.7$ (magnitude in lattice units). Such calculations were used for

616 intrinsic permeability estimation. **(g)** Estimated intrinsic permeability-k (logarithmic scale on

617 y-axis) as a function of crystallinity and scaled to real units with an average crystal grain size

618 of 4 mm [Cheadle et al., 2004]; see equation (2) for the expression of the 3rd order polynomial

619   fit. To show that the chosen matrix volume is a representative elementary volume we compare

620   the intrinsic permeability obtained with a matrix of 160x160x240 l.u. with that of a larger

621   matrix of 320x320x480 l.u., produced with the same algorithm. The two matrices sizes

622   display very similar intrinsic permeability up to ε_x=0.7.

623   **Fig. 3: Initial representative random MVP distribution (2nd boiling scenario).**

624   Calculations for different MVP saturations ($S_g = \varepsilon_g/(1 - \varepsilon_x)$) ($\varepsilon_g$ and ε_x are MVP and crystal

625   volume fraction, respectively) defined as the pore volume fraction occupied by MVP, ($S_g =$ **a)**

626   0.05, **b)** 0.1, **c)** 0.2, **d)** 0.3) equivalent to ε_g = 0.02, 0.04, 0.08, 0.12, respectively) in a crystal

627   matrix with ε_x=0.6. Crystals and melt are transparent. At higher S_g, the effect of solid

628   confinement on bubble shape is stronger.

629   **Figure 4. MVP pore-scale calculations and channels formation. (a&b)** MVP distribution

630   and velocity field **(a&c)** before and **(b&d)** after MVP channels formation with Bo=0.5, ε_x=0.6

631   and ε_g=0.1 (crystalline matrix = gray, silicate melt = transparent). **e)** Occurrence of MVP

632   channels (triangles) versus trapped or slow mobile MVP bubbles (circle). Continuous lines are

633   MVP-saturation ($S_g = \varepsilon_g/(1 - \varepsilon_x)$) contours, that quantifies the pore volume fraction

634   occupied by the MVP. Dashed lines indicate ε_g under isobaric, closed-system, degassing

635   (rhyolite-MELTS; Gualda et al. [2012]). **f)** Critical volume fraction of MVP at Bo=0.1, 0.5, 1.

636   At ε_x=0.6 and Bo=0.1, our calculation shows that a MVP saturation higher than 0.4 has to be

637   reached before MVP can flow through channels.

638   **Fig. 5: MVP injection from below**. **a)** Pore-scale calculation example for MVP fingering and

639   channel formation at three different time snapshots for Bo= 0.5 and ε_x=0.6. h is the thickness

640   of the inlet chamber that is occupied by the MVP only and determines the initial pressure drop

641   which is responsible for winning the resistive capillary forces exerted by the porous medium

642   (critical h for fingering to occur depends on capillary resistivity (i.e. crystal volume fraction)

643   and Bo value). **b)** MVP-ε_g threshold for Bo=0.1, 0.5, 1 for ex-situ scenario.

644   **Fig. 6**: **Injection vs. 2nd boiling-like channel formation, Bo=0.5.** MVP distribution and

645   velocity field at the onset of channels formation for **a)** initial MVP random distribution (i.e.

646   2nd boiling) and **b)** MVP injection from below at ε_x=0.6 and Bo=0.5.

647   **Fig. 7**: **Injection vs. 2nd boiling-like channel formation, Bo=1.** MVP distribution and

648   velocity field (magnitude in lattice units) at the onset of channels formation for **a)** MVP

649   injection from below and **b)** initial MVP random distribution (i.e. 2nd boiling) at ε_x=0.7 and

650   Bo=1.

Fig. 8. MVP discharge and MVP relative permeability at the pore-scale. a) MVP Darcy volume flux U_{og}^{lu} (in lattice units l.u.) and **b)** relative permeability k_r for Bo=0.5. We report data only for calculations where MVP channels formed. Relative permeability is estimated from multiphase fluid flow Darcy's law $k_r = \frac{U_{og}^{lu} \nu_g}{k_{lu}(\Delta \rho g)_{lu}}$, where U_{og}^{lu} is the evaluated MVP volume flux (Fig. 8a) , ν_g the simulated MVP viscosity in l.u. and k_{lu} the intrinsic permeability as reported in Fig. 2g, but rescaled to l.u. ($k_{lu} = k/\Delta x^2$).

Figure 9. MVP transport: Modes of MVP transport in reservoir-scale model. The black area highlighted in red is based on pore-scale parametrization for MVP channel formation we obtained for Bo=0.5 (see eq.(1)).

Figure 10. Time evolution of crystal content in the reservoir model: calculations conducted to determine the effects on outgassing of (a) the temperature dependent visco-elastic rheology of the crust surrounding the chamber and (b) the initial size of the chamber. Time is normalized by the cooling time scale $\tau_c = R^2/\kappa$, where R is the initial radius of the reservoir and the κ thermal diffusivity of the crust.

Figure 11. MVP transport at the reservoir scale: (a&c) total volatile mass fraction and **(b&d)** volatile mass fraction loss with respect to binned crystal volume fraction ε_x, for different crust viscosity (**a&b,** initial reservoir volume 50 km^3) and initial reservoir volume (**c&d**, crust viscosity 5x10^{17} Pa s). Black line = theoretical limit (perfectly viscous crust) where the loss of MVP is set by the critical MVP volume fraction. (**a&b**) As the crust viscosity increases, outgassing becomes limited by the pressure difference between the reservoir and the surrounding crust (see Fig. 12a&b). (**c&d**) In small reservoirs, the crust responds elastically to MVP loss, which impedes outgassing (see Fig. 12c&d). The gray area highlights crystal volume fraction above which MVP bubble migration and gas finger formation via capillary invasion is no-longer a viable mechanism for MVP outgassing.

Fig. 12 Thermomechanical chamber model: importance of the thermal state of the crust and chamber size: (a-c) Overpressure, and **(b-d)** MVP volume fraction for varying crust viscosity (**a-b**) and initial chamber volume (**c-d**). As in Fig. 11, the black line denotes the saturation limit. Pressure evolution in (a) during the reservoir scale calculations can be read as follow: (1) slow outgassing due to individual bubble rise; (2) rapid outgassing due to the presence of gas channels; (3) outgassing is hindered by the pressure drop in the chamber; (4) decrease in outgassing due to approach of MVP channel threshold with slight overshoot; (5)

683   outgassing is limited due to MVP channel threshold/saturation limit; (6) outgassing by gas

684   channels ceases. Steps 4 and 5 only occur for a compliant crust and/or large chamber.

685   **LIST OF TABLES:**

686   **Table 1. List of parameters used for pore-scale LB calculations based on the color**

687   **gradient method (CGM).** Physical parameters such as kinematic viscosity and surface

688   tension are reported in lattice units (l.u.).

689   **Table 2. Initial parameter choice for reservoir model calculations.**

690 **References**

691 Anderson, A. T., G. H. Swihart, G. Artioli, and C. A. Geiger (1984), Segregation vesicles, gas

692 filter-pressing, and igneous differentiation, *Journal of Geology*, *92*, 55-72.

693 Annen, C., J. D. Blundy, and R. S. J. Sparks (2006), The genesis of intermediate and silicic

694 magmas in deep crustal hot zones, *Journal of Petrology*, *47*(3), 505-539.

695 Avrami, M. (1939), Kinetics of phase change. I General theory, *The Journal of Chemical*

696 *Physics*, *7*(12), 1103-1112.

697 Bachmann, O., and G. W. Bergantz (2003), Rejuvenation of the Fish Canyon magma body: A

698 window into the evolution of large-volume silicic magma systems, *Geology*, *31*(9), 789-792.

699 Bachmann, O., and G. W. Bergantz (2004), On the origin of crystal-poor rhyolites: Extracted

700 from batholithic crystal mushes, *Journal of Petrology*, *45*(8), 1565-1582.

701 Bachmann, O., and G. W. Bergantz (2008), The Magma Reservoirs That Feed

702 Supereruptions, *Elements*, *4*, 17-21.

703 Bachmann, O., and C. Huber (2016), Silicic magma reservoirs in the Earth's crust, *American*

704 *Mineralogist*, *101*(11), 2377-2404.

705 Barker, G., and A. Mehta (1992), Vibrated powders: structure, correlations, and dynamics,

706 *Physical Review A*, *45*(6), 3435.

707 Blundy, J., K. V. Cashman, A. Rust, and F. Witham (2010), A case for CO2-rich arc magmas,

708 *Earth and Planetary Science Letters*, *290*(3-4), 289-301.

709 Boudreau, A. (2016), Bubble migration in a compacting crystal-liquid mush, *Contrib Mineral*

710 *Petr*, *171*(4).

711 Candela, P. A. (1991), Physics of aqueous phase evolution in plutonic environments,

712 *American Mineralogist*, *76*, 1081-1091.

713 Candela, P. A. (1994), Combined Chemical and Physical Model for Plutonic Devolatilization

714 - a Non-Rayleigh Fractionation Algorithm, *Geochimica Et Cosmochimica Acta*, *58*(10), 2157-

715 2167.

716 Candela, P. A. (1997), A review of shallow, ore-related granites: Textures, volatiles, and ore

717 metals, *Journal of Petrology*, *38*(12), 1619-1633.

718 Caricchi, L., and J. Blundy (2015), Experimental petrology of monotonous intermediate

719 magmas, *Geological Society, London, Special Publications*, *422*.

720 Cheadle, M., M. Elliott, and D. McKenzie (2004), Percolation threshold and permeability of

721 crystallizing igneous rocks: The importance of textural equilibrium, *Geology*, *32*(9), 757-760.

722 Chelle-Michou, C., B. Rottier, L. Caricchi, and G. Simpson (2017), Tempo of magma

723 degassing and the genesis of porphyry copper deposits, *Scientific Reports*, *7*, 40566.

724 Chopard, B., A. Dupuis, A. Masselot, and P. Luthi (2002), Cellular automata and lattice
725 Boltzmann techniques: An approach to model and simulate complex systems, *Advances in*
726 *complex systems*, *5*(02n03), 103-246.

727 Cooper, K. M., and A. J. R. Kent (2014), Rapid remobilization of magmatic crystals kept in
728 cold storage, *Nature*, *506*(7489), 480-483.

729 Degruyter, W., and C. Huber (2014), A model for eruption frequency of upper crustal silicic
730 magma chambers, *Earth and Planetary Science Letters*, *403*(0), 117-130.

731 Degruyter, W., A. Burgisser, O. Bachmann, and O. Malaspinas (2010), Synchrotron X-ray
732 microtomography and lattice Boltzmann simulations of gas flow through volcanic pumices,
733 *Geosphere*, *6*(5), 470-481.

734 Degruyter, W., C. Huber, O. Bachmann, K. M. Cooper, and A. J. R. Kent (2016), Magma
735 reservoir response to transient recharge events: The case of Santorini volcano (Greece),
736 *Geology*, *44*(1), 23-26.

737 Dragoni, M., and C. Magnanensi (1989), Displacement and Stress Produced by a Pressurized,
738 Spherical Magma Chamber, Surrounded by a Viscoelastic Shell, *Phys Earth Planet In*, *56*(3-
739 4), 316-328.

740 Edmonds, M., A. Brett, R. Herd, M. Humphreys, and A. Woods (2015), Magnetite-bubble
741 aggregates at mixing interfaces in andesite magma bodies, *Geological Society, London,*
742 *Special Publications*, *410*(1), 95-121.

743 Eriksen, F. K., R. Toussaint, K. J. Måløy, and E. G. Flekkøy (2015), Invasion patterns during
744 two-phase flow in deformable porous media, *Frontiers in Physics*, *3*, 81.

745 Faroughi, S., and C. Huber (2015), Unifying the relative hindered velocity in suspensions and
746 emulsions of nondeformable particles, *Geophysical research Letters*, *42*(1), 2014GL062570.

747 Faroughi, S., and C. Huber (2016), A predictive viscosity model for concentrated suspensions
748 of rigid, randomly oriented spheroids, *accepted*.

749 Gardner, J. E., and M.-H. Denis (2004), Heterogeneous bubble nucleation on Fe-Ti oxide
750 crystals in high-silica rhyolitic melts, *Geochimica et Cosmochimica Acta*, *68*(17), 3587-3597.

751 Gelman, S. E., F. J. Gutierrez, and O. Bachmann (2013), On the longevity of large upper
752 crustal silicic magma reservoirs, *Geology*, *41*(7), 759-762.

753 Gerlach, T. M. (1991), Present-day CO2 emissions from volcanos, *Eos, Transactions*
754 *American Geophysical Union*, *72*(23), 249-255.

755 Gualda, G. A. R., M. S. Ghiorso, R. V. Lemons, and T. L. Carley (2012), Rhyolite-MELTS:
756 A modified calibration of MELTS optimized for silica-rich, fluid-bearing magmatic systems,
757 *Journal of Petrology*, *53*(5), 875-890.

Gutierrez, F., I. Payacan, S. E. Gelman, O. Bachmann, and M. A. Parada (2013), Late-stage magma flow in a shallow felsic reservoir: Merging the anisotropy of magnetic susceptibility record with numerical simulations in La Gloria Pluton, central Chile, *Journal of Geophysical Research-Solid Earth*, *118*(5), 1984-1998.

Hammer, J. E. (2004), Crystal nucleation in hydrous rhyolite: Experimental data applied to classical theory, *American Mineralogist*, *89*(11-12), 1673-1679.

Heinrich, C. A., and P. A. Candela (2012), Fluids and Ore Formation in the Earth's Crust, *Treatise on Geochemistry, ed. 2*, *13*, 1-28.

Hersum, T. G., and B. D. Marsh (2006), Igneous microstructures from kinetic models of crystallization, *Journal of Volcanology and Geothermal Research*, *154*(1-2), 34-47.

Hess, K. U., and D. B. Dingwell (1996), Viscosities of hydrous leucogranitic melts: A non-Arrhenian model, *American Mineralogist*, *81*(9-10), 1297-1300.

Hildreth, W. S. (2004), Volcanological perspectives on Long Valley, Mammoth Mountain, and Mono Craters: several contiguous but discrete systems, *Journal of Volcanology and Geothermal Research*, *136*(3-4), 169-198.

Hinedi, Z., A. Chang, M. Anderson, and D. Borchardt (1997), Quantification of microporosity by nuclear magnetic resonance relaxation of water imbibed in porous media, *Water Resources Research*, *33*(12), 2697-2704.

Holtzman, R., M. L. Szulczewski, and R. Juanes (2012), Capillary fracturing in granular media, *Physical review letters*, *108*(26), 264504.

Huber, O. Bachmann, and M. Manga (2009), Homogenization processes in silicic magma chambers by stirring and mushification (latent heat buffering), *Earth and Planetary Science Letters*, *283*(1-4), 38-47.

Huber, Bachmann, and Manga (2010), Two Competing Effects of Volatiles on Heat Transfer in Crystal-rich Magmas: Thermal Insulation vs Defrosting, *Journal of Petrology*, *51*(4), 847-867.

Huber, O. Bachmann, J. L. Vigneresse, J. Dufek, and A. Parmigiani (2012), A physical model for metal extraction and transport in shallow magmatic systems, *Geochemistry Geophysics Geosystems*, *13, Q08003, doi:10.1029/2012GC004042*.

Huber, C., A. Parmigiani, J. Latt, and J. Dufek (2013), Channelization of buoyant nonwetting fluids in saturated porous media, *Water Resources Research*, *49*, 6371-6380.

Huybers, P., and C. Langmuir (2009), Feedback between deglaciation, volcanism, and atmospheric CO 2, *Earth and Planetary Science Letters*, *286*(3), 479-491.

791 Iacovino, K., et al. (2016), Quantifying gas emissions from the "Millennium Eruption" of
792 Paektu volcano, Democratic People's Republic of Korea/China, *Science Advances*, *2*(11).

793 Karakas, O., and J. Dufek (2015), Melt evolution and residence in extending crust: Thermal
794 modeling of the crust and crustal magmas, *Earth and Planetary Science Letters*, *425*(0), 131-
795 144.

796 Karakas, O., W. Degruyter, O. Bachmann, and J. Dufek (2017), Lifetime and size of shallow
797 magma bodies controlled by crustal-scale magmatism, *Nature Geosci*, *advance online*
798 *publication*.

799 Leclaire, A. Parmigiani, O. Malaspinas, B. Chopard, and J. Latt (2017), Generalized three-
800 dimensional lattice Boltzmann color-gradient method for immiscible two-phase pore-scale
801 imbibition and drainage in porous media *Physical Review E, 95(3), 033306.*

802 Leclaire, S., M. Reggio, and J.-Y. Trépanier (2012), Numerical evaluation of two recoloring
803 operators for an immiscible two-phase flow lattice Boltzmann model, *Applied Mathematical*
804 *Modelling*, *36*(5), 2237-2252.

805 Leclaire, S., N. Pellerin, M. Reggio, and J. Y. Trépanier (2015), An approach to control the
806 spurious currents in a multiphase lattice Boltzmann method and to improve the
807 implementation of initial condition, *International Journal for Numerical Methods in Fluids*,
808 *77*(12), 732-746.

809 Leclaire, S., N. Pellerin, M. Reggio, and J.-Y. Trépanier (2016), A multiphase lattice
810 Boltzmann method for simulating immiscible liquid-liquid interface dynamics, *Applied*
811 *Mathematical Modelling*, *40*(13–14), 6376-6394.

812 Lee, C.-T. A., and D. M. Morton (2015), High silica granites: Terminal porosity and crystal
813 settling in shallow magma chambers, *Earth and Planetary Science Letters*, *409*, 23-31.

814 Lemmon, E. W., M. O. McLinden, and D. G. Friend (2003), *Thermophysical Properties of*
815 *Fluid Systems*, Gaithersburg MD, 20899.

816 Li, Y., Y. Xu, and C. Thornton (2005), A comparison of discrete element simulations and
817 experiments for 'sandpiles' composed of spherical particles, *Powder Technology*, *160*(3),
818 219-228.

819 Lipman (2007), Incremental assembly and prolonged consolidation of Cordilleran magma
820 chambers: Evidence from the Southern Rocky Mountain Volcanic Field, *Geosphere*, *3*(1), 1-
821 29.

822 Lipman, P. W., and O. Bachmann (2015), Ignimbrites to batholiths: Integrating perspectives
823 from geological, geophysical, and geochronological data, *Geosphere*.

824 Liu, H., Q. Kang, C. R. Leonardi, S. Schmieschek, A. Narváez, B. D. Jones, J. R. Williams,
825 A. J. Valocchi, and J. Harting (2016), Multiphase lattice Boltzmann simulations for porous
826 media applications, *Computational Geosciences*, 1-29.

827 London, D., and G. B. Morgan (2012), The pegmatite puzzle, *Elements*, *8*(4), 263-268.

828 Mangan, M., and T. W. Sisson (2005), Evolution of melt-vapor surface tension in silicic
829 volcanic systems: Experiments with hydrous melts, *J. geophys. Res.*, *110, B01202,*
830 *doi:10.1029/2004JB003215.*

831 Marsh (1989), Magma chambers, *Annual Review of Earth and Planetary Sciences*, *17*, 439-
832 474.

833 Marsh, B. D. (1981), On the crystallinity, probability of occurrence, and rheology of lava and
834 magma, *Contrib Mineral Petr*, *78*, 85-98.

835 Menand, T., C. Annen, and M. de Saint Blanquat (2015), Rates of magma transfer in the
836 crust: Insights into magma reservoir recharge and pluton growth, *Geology*, *43*(3), 199-202.

837 Miller, C. F., D. J. Furbish, B. A. Walker, L. L. Claiborne, G. C. Koteas, H. A. Bleick, and J.
838 S. Miller (2011), Growth of plutons by incremental emplacement of sheets in crystal-rich
839 host: Evidence from Miocene intrusions of the Colorado River region, Nevada, USA,
840 *Tectonophysics*, *500*(1-4), 65-77.

841 Mungall, J. E. (2015), Physical Controls of Nucleation, Growth and Migration of Vapor
842 Bubbles in Partially Molten Cumulates, 331-377.

843 Navon, O., and V. Lyakhovsky (1998), Vesiculation processes in silicic magmas, in *The*
844 *physics of volcanic eruptions*, edited by J. S. Gilbert and R. S. J. Sparks, pp. 27-50,
845 Geological Society, London.

846 Ngachin, M., R. G. Galdamez, S. Gokaltun, and M. C. Sukop (2015), Lattice Boltzmann
847 simulation of rising bubble dynamics using an effective buoyancy method, *International*
848 *Journal of Modern Physics C*, *26*(03), 1550031.

849 Oppenheimer, J., A. Rust, K. Cashman, and B. Sandnes (2015), Gas migration regimes and
850 outgassing in particle-rich suspensions, *Front. Phys. 3: 60. doi: 10.3389/fphy*.

851 Paonita, A. (2005), Noble gas solubility in silicate melts: a review of experimentation and
852 theory, and implications regarding magma degassing processes, *Annals of Geophysics*.

853 Paonita, A., A. Caracausi, M. Martelli, and A. L. Rizzo (2016), Temporal variations of helium
854 isotopes in volcanic gases quantify pre-eruptive refill and pressurization in magma reservoirs:
855 The Mount Etna case, *Geology*, *44*(7), 499-502.

856 Parmigiani, A., C. Huber, and O. Bachmann (2014), Mush microphysics and the reactivation

857 of crystal-rich magma reservoirs, *Journal of Geophysical Research: Solid Earth*, *119*(8),

858 6308-6322.

859 Parmigiani, A., C. Huber, O. Bachmann, and B. Chopard (2011), Pore-scale mass and reactant

860 transport in multiphase porous media flows, *Journal of Fluid Mechanics*, *686*, 40-76.

861 Parmigiani, A., S. Faroughi, C. Huber, O. Bachmann, and Y. Su (2016), Bubble accumulation

862 and its role in the evolution of magma reservoirs in the upper crust, *Nature*, *532*(7600), 492-

863 495.

864 Pistone, M., et al. (2015), Gas-driven filter pressing in magmas: Insights into in-situ melt

865 segregation from crystal mushes, *Geology*, *43*(8), 699-702.

866 Plank, T., K. A. Kelley, M. M. Zimmer, E. H. Hauri, and P. J. Wallace (2013), Why do mafic

867 arc magmas contain ~ 4 wt% water on average?, *Earth and Planetary Science Letters*, *364*(0),

868 168-179.

869 Reis, T., and T. Phillips (2007), Lattice Boltzmann model for simulating immiscible two-

870 phase flows, *Journal of Physics A: Mathematical and Theoretical*, *40*(14), 4033.

871 Ren, F., B. Song, and M. C. Sukop (2016), Terminal shape and velocity of a rising bubble by

872 phase-field-based incompressible Lattice Boltzmann model, *Advances in Water Resources*,

873 *97*, 100-109.

874 Shampine, L. F., and M. W. Reichelt (1997), The matlab ode suite, *SIAM journal on scientific

875 computing*, *18*(1), 1-22.

876 Shin, H., and J. C. Santamarina (2010), Fluid-driven fractures in uncemented sediments:

877 Underlying particle-level processes, *Earth and Planetary Science Letters*, *299*(1–2), 180-189.

878 Shinohara (2008), Excess degassing from volcanoes and its role on eruptive and intrusive

879 activity, *Reviews of Geophysics*, *46, RG4005*.

880 Shinohara (2013), Volatile flux from subduction zone volcanoes: Insights from a detailed

881 evaluation of the fluxes from volcanoes in Japan, *Journal of Volcanology and Geothermal

882 Research*, *268*, 46-63.

883 Sillitoe, R. H. (2010), Porphyry Copper Systems, *Economic Geology*, *105*(1), 3-41.

884 Sisson, T. W., and C. R. Bacon (1999), Gas-driven filter pressing in magmas, *Geology*, *27*(7),

885 613-616.

886 Soden, B. J., R. T. Wetherald, G. L. Stenchikov, and A. Robock (2002), Global Cooling After

887 the Eruption of Mount Pinatubo: A Test of Climate Feedback by Water Vapor, *Science*,

888 *296*(5568), 727-730.

889 Spina, L., C. Cimarelli, B. Scheu, D. Di Genova, and D. B. Dingwell (2016), On the slow

890 decompressive response of volatile- and crystal-bearing magmas: An analogue experimental

891 investigation, *Earth and Planetary Science Letters*, *433*, 44-53.

892 Stöhr, M., and A. Khalili (2006), Dynamic regimes of buoyancy-affected two-phase flow in

893 unconsolidated porous media, *Physical Review E*, *73*(3), 036301.

894 Thomas, R., and P. Davidson (2013), The missing link between granites and granitic

895 pegmatites, *Journal of Geosciences*, *58*(2), 183.

896 Vidal, C. M., N. Métrich, J.-C. Komorowski, I. Pratomo, A. Michel, N. Kartadinata, V.

897 Robert, and F. Lavigne (2016), The 1257 Samalas eruption (Lombok, Indonesia): the single

898 greatest stratospheric gas release of the Common Era, *Scientific Reports*, *6*.

899 Wallace, P. J. (2005), Volatiles in subduction zone magmas: concentrations and fluxes based

900 on melt inclusion and volcanic gas data, *Journal of Volcanology and Geothermal Research*,

901 *140*(1-3), 217-240.

902 Ward, K. M., G. Zandt, S. L. Beck, D. H. Christensen, and H. McFarlin (2014), Seismic

903 imaging of the magmatic underpinnings beneath the Altiplano-Puna volcanic complex from

904 the joint inversion of surface wave dispersion and receiver functions, *Earth and Planetary*

905 *Science Letters*, *404*(0), 43-53.

906 Weinberg, R. F. (1999), Mesoscale pervasive felsic magma migration: alternatives to dyking,

907 *Lithos*, *46*(3), 393-410.

908 Weinberg, R. F., and K. Regenauer-Lieb (2010), Ductile fractures and magma migration from

909 source, *Geology*, *38*(4), 363-366.

910 Weis, P., T. Driesner, and C. Heinrich (2012), Porphyry-copper ore shells form at stable

911 pressure-temperature fronts within dynamic fluid plumes, *Science*, *338*(6114), 1613-1616.

912 Westrich, H. R., and T. M. Gerlach (1992), Magmatic gas source for the stratospheric SO2

913 cloud from the June 15,1991, eruption of Mount Pinatubo, *Geology*, *20*(10), 867-870.

914 White, S. M., J. A. Crisp, and F. A. Spera (2006), Long-term volumetric eruption rates and

915 magma budgets, *Geochem. Geophys. Geosyst.*, *7*(doi:10.1029/2005GC001002).

916 Whitney, J. A. (1988), The origin of granite: The role and source of water in the evolution of

917 granitic magmas, *Geological Society of America Bulletin*, *100*(12), 1886-1897.

918 Zellmer, G. F., M. Edmonds, and S. M. Straub (2015), Volatiles in subduction zone

919 magmatism, *Geological Society, London, Special Publications*, *410*(1), 1-17.

Figure 1.

LB - PORE SCALE
periodic boundary
periodic boundary
periodic boundary
periodic boundary
MVP buoyancy

MVP loss

Heat loss

a

b

Bubble accumulation in melt-rich pockets and
magma recharge not modeled in this paper
(see Parmigiani et al., 2016, Degruyter et al., 2016)
1: Caldera systems (e.g., Taupo, NZ; SRMVF, USA)
2: Stratovolcanoes (e.g., Nisyros, Greece; Mt St. Helens, USA)

RESERVOIR MODEL
1. outgassing
5. heat loss to the crust
2. visco elastic crust
3. crystallization
4. exsolution

Figure 2.

a. $\varepsilon_x \sim 0.4$

b. $\varepsilon_x \sim 0.5$

e. velocity $\varepsilon_x \sim 0.6$

vel 1.2e-2

8e-3

4e-3

0.

f. velocity $\varepsilon_x \sim 0.7$

vel 6e-3

4e-3

2e-3

0.

c. $\varepsilon_x \sim 0.6$

d. $\varepsilon_x \sim 0.7$

g.

160x160x240 l.u.
3rd order poly. fit
320x320x480 l.u.

$\Delta x \sim 4mm$ (crystal grain size)

permeability m^2

crystal volume fraction

Figure 3.

MVP Sg~0.05

a.

MVP Sg~0.1

b.

MVP Sg~0.2

c.

MVP Sg~0.3

d.

Figure 4.

a. MVP-distribution
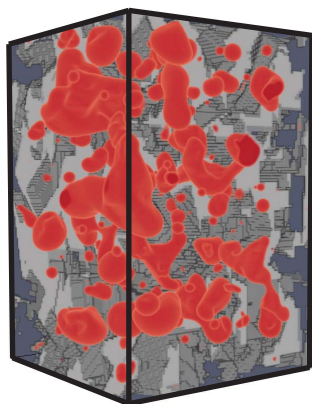
c. MVP-velocity
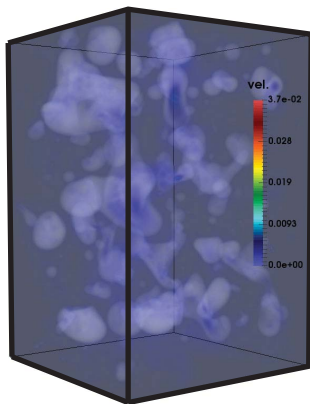
Before MVP channels formation

b.

d.

After MVP channels formation

e. Bo=0.5   2nd boiling

MELTS 7 wt. % H2O, 2 kbar

MELTS 4 wt. % H2O, 2 kbar

YES channel
NO channel

Sg=0.4
Sg=0.3
Sg=0.2
Sg=0.1

MVP volume fraction

crystal volume fraction

f.   2nd boiling

MELTS 7 wt. % H2O, 2 kbar

MELTS 4 wt. % H2O, 2 kbar

Bo=0.1
Bo=0.5
Bo=1.

MVP volume fraction

crystal volume fraction

Figure 5.

a. **Bo=0.5; $\varepsilon_x \sim 0.6$**

b. MVP injection

Figure showing MVP volume fraction vs crystal volume fraction with legend:
Bo=0.1 (green), Bo=0.5 (black), Bo=1. (blue)

MELTS 7 wt. % H2O, 2 kbar

MELTS 4 wt. % H2O, 2 kbar

Sg=0.4, Sg=0.3, Sg=0.2, Sg=0.1

Figure 6.

Bo=0.5; $\varepsilon_x \sim 0.6$

a.

MVP vol. fraction ~0.07

2nd boiling

b.
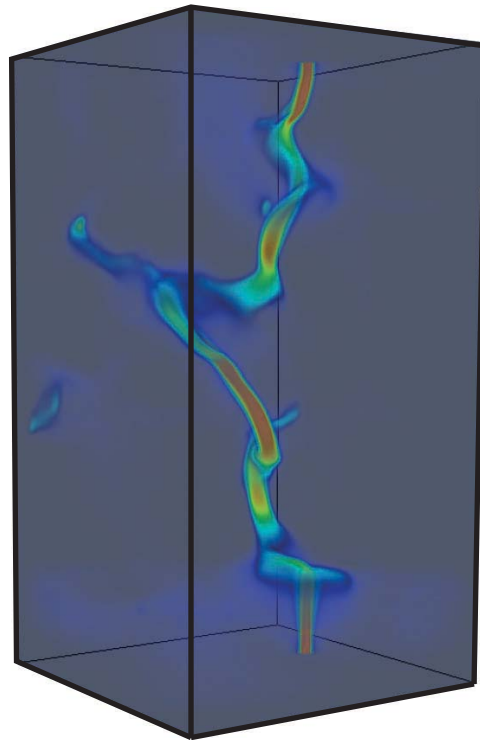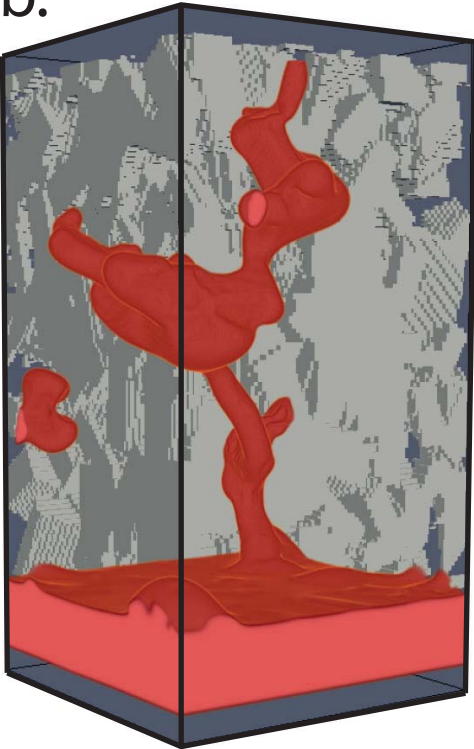
MVP vol. fraction~0.045

MVP injection

Figure 7.

MVP injection

2nd boiling

a.

b.

MVP vol. fraction~3.6%;

MVP vol. fraction~7.5%

vel

4.3e-2

2.8e-2

1.4e-2

0.

$Bo=1; \varepsilon_x \sim 0.7$

Figure 8.

a.

b.

Figure 9.

> potential for capillary fracruting

MVP channel

trapped bubbles

crystal volume fraction

MVP volume fraction

0

0.2

0.4

0.6

0.8

0

0.8

0.6

0.4

0.2

0

0   0.2   0.4   0.6   0.8

melt volume fraction

MVP is the carrier phase

bubbles & crystal suspension

Figure 10.

Figure 11.

a.

bubbles & crystal
suspension

MVP channel

> potential for fracturing

saturation limit
5e17 Pa s (300 °C)
5e18 Pa s (250 °C)

b.

> potential for fracturing

c.

5 km³
10 km³
50 km³
100 km³
500 km³
saturation limit

> potential for fracturing

d.

> potential for fracturing

Figure 12.

symbol	Definition	Value
Bo	Bond number : $(g\Delta\rho)_{lu}$ $D_{lu}{}^2 / \sigma_{lu}$	0.1-1
$(g\Delta\rho)_{lu}$	body force-buoyancy in l.u. applied to MVP only	5e-6 - 5e-5
D_{lu}	average pore diameter in l.u.	10
σ_{lu}	surface tension in l.u.	5e-3
β	constant for thickness of diffuse interface	0.7
ε_x	crystal volume fraction	0.4 - 0.75
ε_g	MVP volume fraction	0.015 - 0.15
ν_b, ν_m	kinematic viscosity wetting phase ("melt") in l.u	0.5
τ_b	relaxation time for wetting phase	2
M	viscosity ratio: ν_r / ν_b	1/100
ν_r, ν_g	kinematic viscosity non-wetting phase ("MVP"): ν_bM	0.005
τ_r	relaxation time for non-wetting phase	0.515

Table 1

symbol	Definition	Value	Units
P_{lith}	lithostatic pressure	200	MPa
P_{ini}	initial chamber pressure	200	MPa
T_l	liquidus temperature	1020	°C
T_s	solidus temperature	700	°C
T_{ini}	initial chamber temperature	850	°C
T_c	temperature at the outer boundary of the visco-elastic crust	250-300	°C
∇T	geothermal gradient	~30	°C/km
b	power law exponent melting curve [*Huber et al.*, 2010]	0.5	
V_{ini}	initial chamber volume	5-500	km^3
M_{water}	initial fraction water mass content	5.6	wt %
η_{cold}	dynamic viscosity of the crust at T_c=250 °C	5.00e+17	Pa s
η_{hot}	dynamic viscosity of the crust at T_c=300 °C	5.00e+18	Pa s
κ	thermal diffusivity of the crust	1e-6	m^2/s
L_e	latent heat of exsolution [*Caricchi & Blundy*, 2015]	610e+3	J/Kg
L_m	latent heat of melting [*Caricchi & Blundy*, 2015]	290e+3	J/Kg

Table2